

## Adaptive Kinetic Monte Carlo Simulations of Surface Segregation in PdAu Nanoparticles

Lei Li<sup>†</sup>, Xinyu Li<sup>†</sup>, Zhiyao Duan<sup>†</sup>, Randall J. Meyer<sup>‡</sup>, Rob Carr<sup>‡</sup>, Sumathy Raman<sup>‡</sup>, Lucas Koziol<sup>‡\*</sup>, and Graeme Henkelman<sup>‡\*</sup>

<sup>†</sup>Department of Chemistry and the Institute for Computational Engineering and Sciences, University of Texas at Austin, Austin, Texas 78712-0231, United States

<sup>‡</sup>Corporate Strategic Research, ExxonMobil Research and Engineering Company, 1545 US Route 22 East, Annandale, NJ 08801, United States

### Abstract

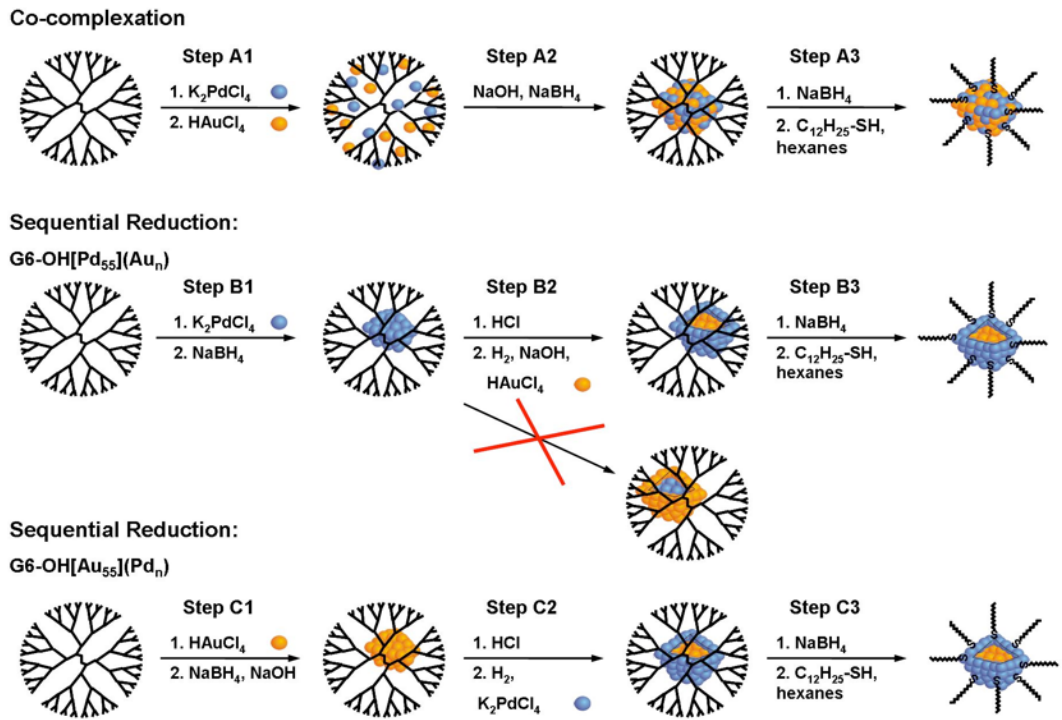
Surface segregation in bimetallic nanoparticles (NPs) is critically important for their catalytic activity because the activity is largely determined by the surface composition. Little, however, is known about the atomic scale mechanisms and kinetics of surface segregation. One reason is that it is hard to resolve atomic rearrangements experimentally. It is also difficult to model surface segregation at the atomic scale because the atomic rearrangements can take place on time scales of seconds or minutes – much longer than can be modeled with molecular dynamics. Here we use the adaptive kinetic Monte Carlo (AKMC) method to model the segregation dynamics in PdAu NPs over experimentally relevant time scales, and reveal the origin of kinetic stability of the core@shell and random alloy NPs at the atomic level. Our focus on PdAu NPs is motivated by experimental work showing that both core@shell and random alloy PdAu NPs with diameters of less than 2 nm are stable, indicating that one of these structures must be metastable and kinetically trapped. Our simulations show that both the Au@Pd and the PdAu random alloy NPs are metastable and kinetically trapped below 400 K over time scales of hours. These AKMC simulations provide insight into the energy landscape of the two NP structures, and the diffusion mechanisms that lead to segregation. In the core-shell NP, surface segregation occurs primarily on the (100) facet through both a vacancy-mediated and a concerted mechanism. The system becomes kinetically trapped when all corner sites in the core of the NP are occupied by Pd atoms. Higher energy barriers are required for further segregation, so that the metastable NP has a partially alloyed shell. In contrast, surface segregation in the random alloy PdAu NP is suppressed because the random alloy NP has reduced strain as compared to the Au@Pd NP, and the segregation mechanisms in the alloy require more elastic energy for exchange of Pd and Au and between the surface and subsurface.

## Introduction

Bimetallic nanoparticles (NPs) can exhibit superior catalytic activity and enhanced selectivity as compared to their monometallic counterparts due to synergistic effects that have been widely investigated in both heterogeneous thermal catalysis and electrocatalysis.<sup>1-5</sup> Since catalytic processes occur directly on the surface of bimetallic NPs, the surface composition, structure, and the local order of atoms on bimetallic NPs have profound influence on their catalytic performance.<sup>6</sup>

<sup>15</sup> Surfaces of bimetallic NPs are sensitive to the environment and can undergo redistribution of the atomic species under reaction conditions.<sup>16-22</sup> One profound change is the segregation of one component on the surface – surface segregation – that can occur during preparation, pretreatment, and even under reaction conditions.<sup>16,23-26</sup> Compositional changes and local rearrangement of species on the surface can significantly alter both the electronic and mechanical properties of NPs, impacting catalytic activity and selectivity.<sup>27</sup> Control of these properties has been recognized as an effective way to manipulate the activity of bimetallic NPs; understanding the mechanisms of surface segregation is an important step towards being able to control the surface composition and catalytic activity.

PdAu NPs have been widely used in industrial processes including hydrogen peroxide synthesis from H<sub>2</sub> and O<sub>2</sub>,<sup>2,28</sup> alcohol oxidation,<sup>29</sup> vinyl acetate monomer synthesis,<sup>1,10</sup> and formic acid dehydrogenation.<sup>30</sup> The surface composition and structure of PdAu NPs have been shown to significantly affect their catalytic activity and selectivity. Identifying the segregation state of surface species is thus critical to understanding their catalytic function. There are, however, open questions as to the mechanism and even the direction of surface segregation. For example, some experimental studies reported that Au@Pd or Pd@Au core-shell NPs can be synthesized with no surface segregation,<sup>31-34</sup> whereas other studies show that Au segregation occurs during preparation, pretreatment, and even under catalytic conditions.<sup>35-37</sup> In contrast, Enache et al. reported that Pd surface segregation occurs upon calcination, producing NPs with a Pd-rich shell and a Au-rich core.<sup>29</sup> Interestingly, the Crooks' group obtained a set of puzzling results from the synthesis of PdAu NPs (Scheme 1).<sup>38</sup> They found that the sequential reduction of Pd and Au produced Au@Pd core-shell NPs, independent of the reduction order. That is, no matter whether Pd was first reduced and then Au, or Au was first reduced and then Pd, the result was a Au@Pd NP structure. This result alone would not be surprising with the hypothesis that the NP was able to completely invert and find the thermodynamically stable structure corresponding to Au@Pd.



**Scheme 1.** Schematic illustration of the synthesis of PdAu dendrimer-encapsulated NPs. Reproduced with permission. Copyright 2009, American Chemical Society.

What makes this system so interesting is that co-reduction of Pd and Au in the same environment leads to random alloy PdAu NPs with no detectable segregation of either Pd or Au to the surface. Clearly the random alloy and the Au@Pd NP structure can not both be thermodynamically stable and so this raises the question as to which structure is most stable and how the other can be kinetically trapped when NP rearrangement appear to be facile when synthesized via sequential reductions. These interesting and puzzling results motivated our theoretical exploration of the surface segregation of AuPd NPs.

Some previous theoretical work investigated surface segregation in bimetallic NPs, including calculations of segregation energies with density functional theory (DFT); equilibrium-state predictions based upon empirical thermodynamic models and Monte Carlo sampling; and dynamical simulations based upon molecular dynamics (MD) methods.<sup>39-47</sup> The first two methods are used to predict equilibrium configurations of bimetallic NPs, but not metastable states, where the stability is governed by kinetic factors. The third method, in which MD is used to explore the

evolution of the system, is limited to short time scales (typically  $<\mu\text{s}$ ) – far from the relevant experimental time scales in catalysis.

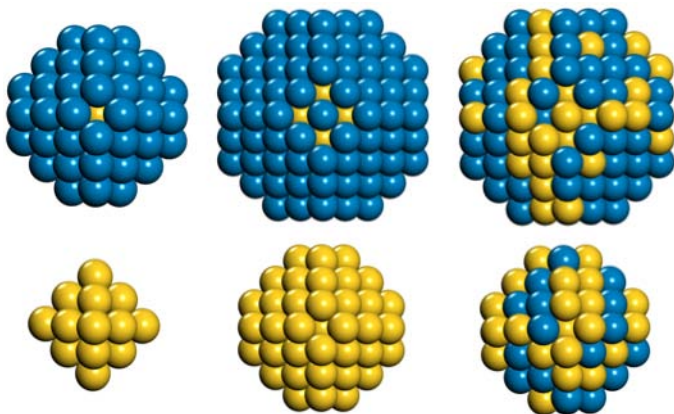


**Figure 1.** Geometric structures of PdAu NP models used in this study,  $\text{Au}_{19}@\text{Pd}_{60}$  and  $\text{Au}_{79}@\text{Pd}_{122}$  core-shell and  $\text{Au}_{79}\text{Pd}_{122}$  random alloy. The lower panel shows the corresponding core structure of each model, with the surface atoms removed. The blue and the gold spheres represent the Pd and the Au atoms, respectively. The same color code is used for all subsequent figures.

To mitigate the time scale problem, we use the AKMC method, in which atomic transition rates are determined by transition state theory (TST) and the time evolution of the system is on the time scale of the state-to-state transitions rather than on the time scale of the molecular vibrations, as in MD. In contrast to the Crook's experiments, where surface Pd is stabilized by adsorbates,<sup>38</sup> our calculations of NPs in vacuum favor the Pd@Au structure, energetically. To model segregation kinetics, we start with the three metastable face-centered-cubic truncated octahedral NP models shown in (Figure 1): 79 atom Au@Pd; 201 atom Au@Pd; and a 201 random alloy AuPd NP. Then, with our AKMC simulations, we determine the mechanism and times scale of segregation in each of these three models to understand why the random alloy remains kinetically trapped over experimental time scales.

## Results

**Surface segregation in  $\text{Au}_{19}@\text{Pd}_{60}$  core-shell NPs.** The dynamical evolution of a truncated-octahedral  $\text{Au}_{19}@\text{Pd}_{60}$  core-shell NP was simulated with the AKMC method (Figure 1 and Movie S1); details of these AKMC calculations are provided in the Computational Methods section. This NP has an energy that is 7.7 eV higher than the global minimum structure as predicted by a Monte

Carlo simulation in which all 19 Au atoms occupy the (100) facet sites of the shell. Thus, segregation of the 19 Au core atoms to the surface of the  $\text{Au}_{19}@\text{Pd}_{60}$  core-shell NP is expected from thermodynamics. However, this structure is not observed in our AKMC simulations; instead, the system reaches a metastable state with six Au atoms segregated to the NP surface.

Figure 2a shows the evolution of the  $\text{Au}_{19}@\text{Pd}_{60}$  core-shell NP measured by the total energy and the number of Au atoms in the shell. The vertical spikes in the energy trace correspond to the formation of short-lived vacancies that diffuse on the surface, which only occasionally facilitate segregation events. Seven energy plateaus are observed in the simulation corresponding to  $n=0-6$  where  $n$  is the number of Au atoms in the NP shell. Each energy drop, of roughly 0.4 eV, corresponds to one Au atom migrating to the shell and one Pd atom migrating to the core. Notably, the migrating shell Pd atom always occupies the corner site of the octahedral core. Such a process leads to the transition of the system from an  $n=k$  to an  $n=k+1$  state, denoted as an  $n=k \rightarrow k+1$  transition. At 32 s, all six corner sites of the core are occupied by Pd atoms, as shown in the upper panel inset of Figure 2a. When the system reaches the  $n=6$  state, the total energy has decreased by 2.24 eV. No further energy drop is observed in 850 s; instead, the energy fluctuates as expected for a system in local equilibrium in a metastable state.

A disconnectivity graph from the first 2000 states is shown in Figure 2b.<sup>48-52</sup> Briefly, the endpoint of each vertical line in a disconnectivity graph corresponds to a stable minimum visited in the AKMC calculation. The vertex which connects any set of vertical line segments indicates the energy of the saddle point(s) that connects the corresponding minima. To make such a plot, there must be some energy discretization, and in this case we have used 0.03 eV. The high energy, black portion of the plot, corresponds to transitions between  $n=0$  and  $n=5$ . The low energy, blue portion, shows the numerous states in which the system becomes trapped when  $n=6$ . These  $n=6$  states are connected via surface rearrangements similar to the two mechanisms shown in Figure 2c. In the first mechanism, three edge Pd atoms slide to produce an adatom-vacancy pair that can easily diffuse on the NP surface. In the second, surface Au atoms migrate from the corner to the facet to the edge site. No exchange between surface-Pd and Au-core atoms occurs in these processes, and the system remains in the  $n=6$  state. In contrast to our (equilibrium) MC simulations, our AKMC simulations show that the  $\text{Au}_{19}@\text{Pd}_{60}$  core@shell NP is kinetically trapped with 13 Au atoms remaining in the core when the six corner sites of the core are occupied by Pd atoms.

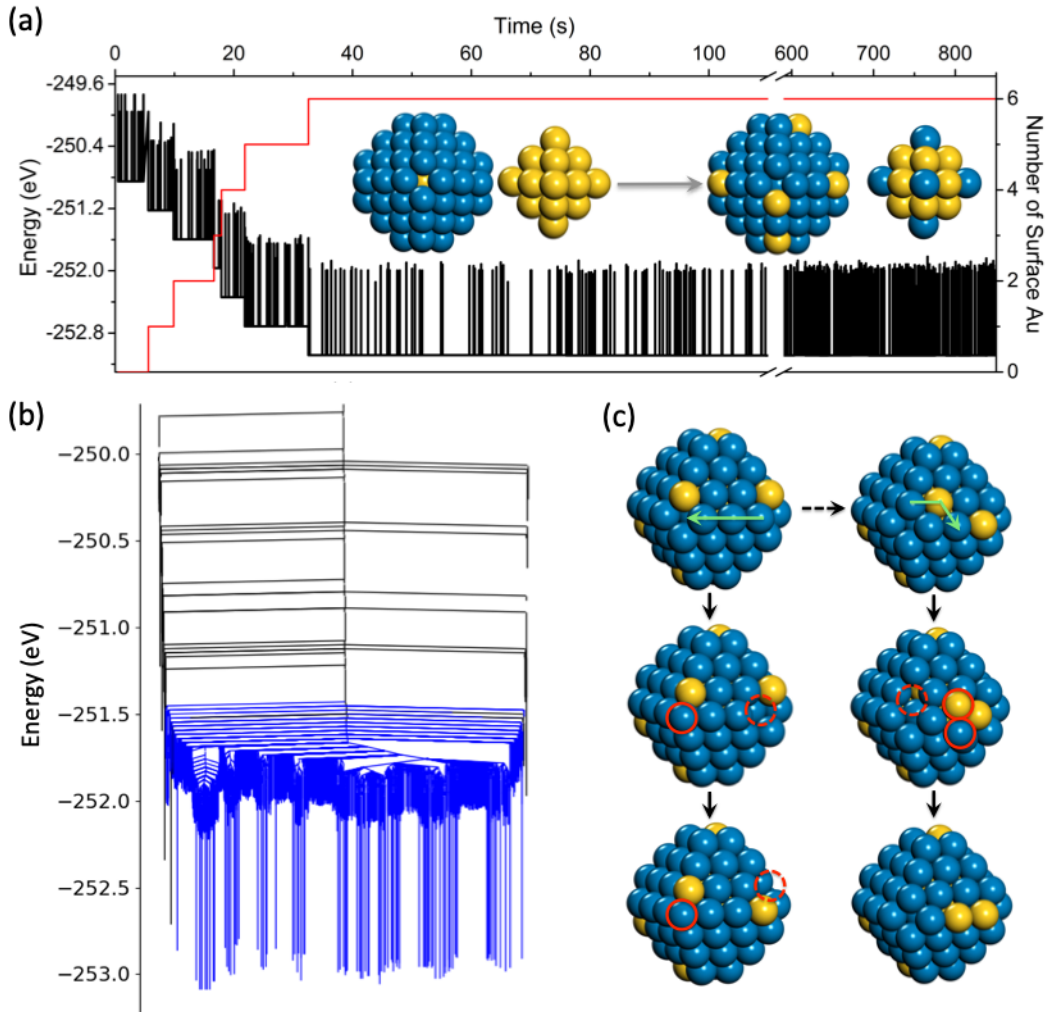


**Figure 2.** (a) The time evolution of the total energy (black line) and the number of the surface Au atoms (red line) in an AKMC simulation of the Au<sub>19</sub>@Pd<sub>60</sub> core@shell NP at 400 K. The inset images show the initial and final structures followed by the corresponding core structures, with the shell atoms removed for visualization purposes. (b) A disconnectivity graph constructed from the first 2000 unique states visited in the AKMC simulation. The  $n=6$  states are highlighted in blue. (c) Two processes involving surface rearrangements between  $n=6$  states: diffusion of a vacancy site (left); and the redistribution of surface Au atoms (right). The green arrows indicate the migration directions of the diffusing atoms. The red solid and dashed circles highlight the adatom and the vacancy sites, respectively.

The qualitative difference between the AKMC and MC simulations indicates the importance of kinetics in surface segregation of Au in PdAu NPs. To further understand the kinetic stabilization, we explored the mechanism by which further segregation can occur beyond the

metastable  $n=6$  state by increasing the simulation temperature. Starting from the metastable ( $n=6$ ) state obtained from our AKMC simulations at 400 K, we performed subsequent AKMC simulations at elevated temperatures between 600 and 900 K. Figure 3a shows the evolution of the total energy and the number of surface Au atoms in an AKMC simulation at 600 K. As indicated by the gray dotted line, a drop in energy is observed at 0.10 s, corresponding to the transition from the  $n=6$  to the  $n=7$  state. In the inset image, a Pd atom is shown to reside beside the six corner sites occupies one of the edge sites in the core, consistent with a segregation event from the  $n=6$  metastable state. In other simulations with temperatures above 600 K, a similar escape mechanism from the  $n=6$  state is observed.

To quantify the kinetics of further segregation beyond the metastable  $n=6$  state, the disconnectivity graph and the temperature dependence of the transition rate are plotted in Figure 3. From the disconnectivity graph, we are able to extract the overall barrier for each  $n=k \rightarrow k+1$  transition, taken to be the energy difference between the minimum-energy structure of the  $k$  state and the transition state that connects to a  $k+1$  state. For example, the overall barriers of 1.09 and 1.18 eV for the  $n=0 \rightarrow 1$  and the  $n=5 \rightarrow 6$  transition, respectively, are indicated by the dashed lines in Figure 3b. In this way, we can see that the  $n=k \rightarrow k+1$  transitions with  $k < 6$  have comparable overall barriers in the range of 1.08 to 1.20 eV. The temperature dependence of the  $n=0 \rightarrow 6$  transition follows the Arrhenius law (Figure 3c) with an apparent activation energy of 1.11 eV, consistent with the overall barriers obtained from the disconnectivity graph. Similar to the  $n=0 \rightarrow 6$  transition, the Arrhenius law holds for the  $n=6 \rightarrow 7$  transition (red dots and line in Figure 3c) with an apparent activation barrier of 1.92 eV; 0.8 eV higher than that required for the  $n=0 \rightarrow 6$  transitions. Notably, surface rearrangements within the  $n=6$  state involve barriers comparable with the  $n=0 \rightarrow 6$  transitions as shown in Figure 2b. Thus, the high-energy barrier for the  $n=6 \rightarrow 7$  transition hinders further segregation of Au atoms from the core to the surface, trapping the system in the  $n=6$  state when the temperature is below 500 K.

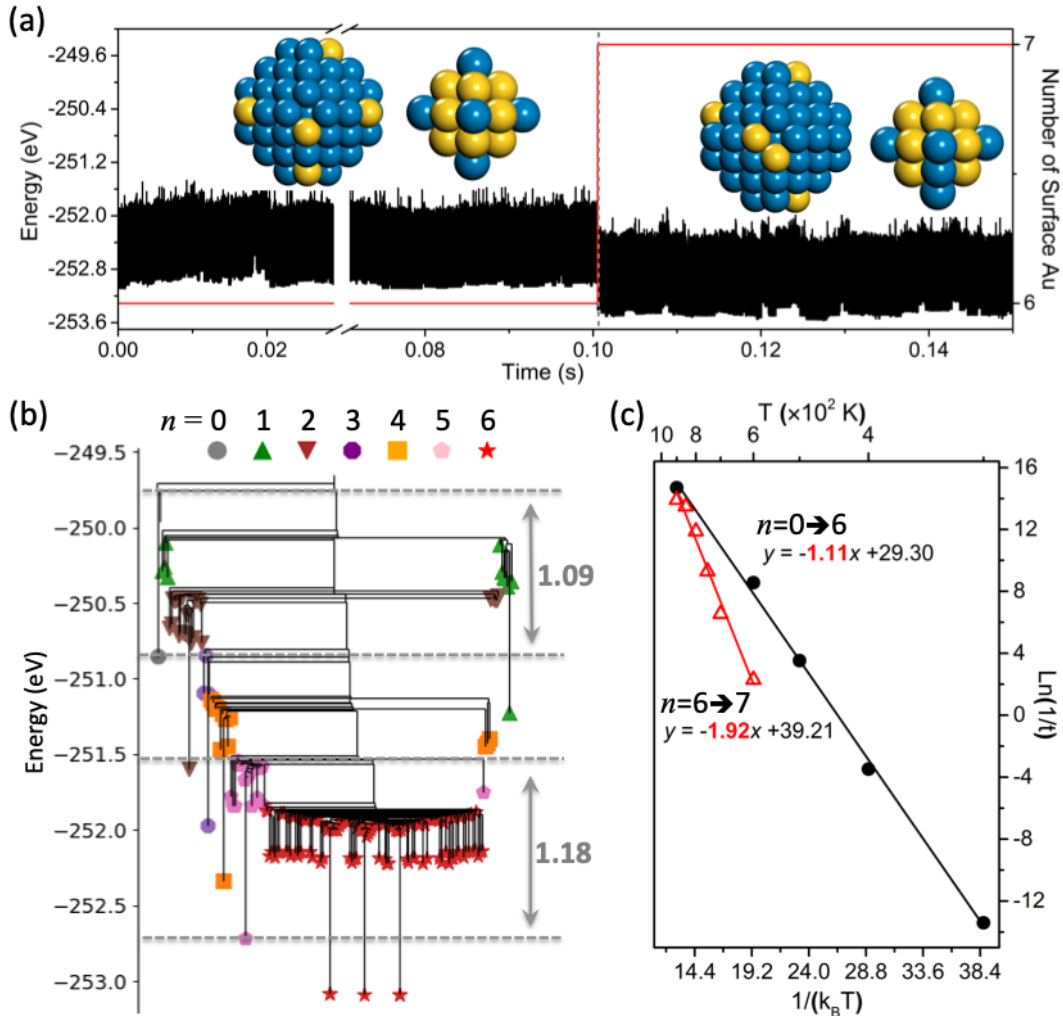


**Figure 3.** (a) Time evolution of the total energy (black line) and the number of surface Au atoms (red line) in an AKMC simulation of a  $\text{Au}_{19}@\text{Pd}_{60}$  core-shell NP at 600 K. The inset images represent the initial and the minima-energy structures followed by the corresponding core structure. (b) Disconnectivity graph for the states found in the AKMC simulation at 400 K up to a time of 35 s with the different  $n$  states indicated by the symbols shown. (c) Arrhenius plots for the  $n=0 \rightarrow 6$  (black line) and  $n=6 \rightarrow 7$  (red line) transitions, where the unit of time is seconds.

The observation that the temperature dependence of the key segregation rates follows the Arrhenius law suggests that there is no change in the mechanism of segregation over the temperature range studied. By looking at each transition, we found that the segregation mechanisms can be classified into two groups: vacancy-mediated, and concerted mechanisms. The vacancy-mediated mechanism, shown in Figure S1, first requires the formation of a vacancy in the

shell, which then facilitates a Au-Pd exchange process. In contrast, in the concerted mechanism, the Au-Pd exchange process occurs directly where the vacancy site is generated simultaneously with the core-to-shell migration of a Au atom. The truncated octahedral structure is then recovered via surface diffusion, which fills the vacancy site. Despite the qualitative differences in these two mechanisms, their overall barriers are comparable and consistent with the activation energy obtained from the Arrhenius plot. Thus, increasing the temperature in our AKMC simulations facilitates escape from the kinetic trap, but does not result in a crossover to another mechanism, up to 900 K. This result suggests that high-temperature AKMC simulations can be used to explore segregation kinetics that are not accessible at the lower temperatures of interest. More importantly, the high-temperature AKMC simulations of the  $\text{Au}_{19}@\text{Pd}_{60}$  NP show that the system is kinetically trapped in a metastable state at 400 K due to kinetic barriers of 1.9 eV.

**Surface segregation in  $\text{Au}_{19}@\text{Pd}_{122}$  core@shell and  $\text{Au}_{19}\text{Pd}_{122}$  alloy NPs.** The kinetic stabilization of the  $\text{Au}_{19}@\text{Pd}_{60}$  NP in the  $n=6$  state demonstrates the importance of kinetics for surface segregation and may resolve the apparent paradoxical results of the Crooks experiments. However, these 79 atom NPs are smaller than those studied in the experiments, where both the Au@Pd core-shell and PdAu alloy NPs were characterized as having an average size of 2.0 nm. A larger  $\text{Au}_{19}@\text{Pd}_{122}$  NP, which also has a size of 2.0 nm, is more representative of those in the experiments. Inspired by our studies on the smaller  $\text{Au}_{19}@\text{Pd}_{60}$  NP, both experimentally relevant (400 K) and elevated ( $\geq 500$  K) temperatures are considered in simulations of the dynamical evolution of the core-shell and alloy NPs. The time evolution of the total energy and the number of Au atoms on the surface for systems at 400 and 800 K, in a typical calculation, are presented in Figures 4 and 5, respectively.

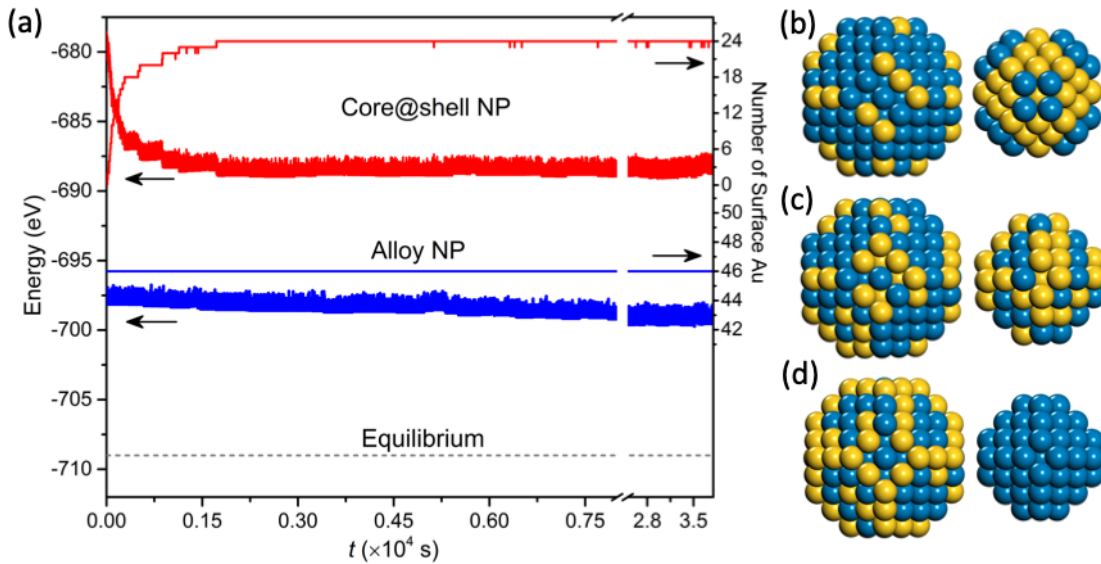


**Figure 4.** The time evolution of the total energy (left axis) and the number of surface Au atoms (right axis) for an AKMC simulations of the  $\text{Au}_{79}@\text{Pd}_{122}$  core-shell (red lines) and the random alloy NP (blue lines) at 400 K. The gray dashed line indicates the equilibrium energy of the global minimum structure calculated from a Monte Carlo simulation. The right panel shows the lowest-energy structures and the corresponding core structures for the (b) core@shell, (c) random alloy, and (d) equilibrium.

At 400 K, early-stage surface segregation of Au atoms was observed in the  $\text{Au}_{79}@\text{Pd}_{122}$  core@shell NP (Movie S2), whereas the random alloy NP maintains the original core structure with no Au-Pd segregation. As shown in Figure 4 (red lines), the core@shell system reaches the  $n=24$  state at  $1.7 \times 10^4$  s (half an hour) with 24 Au atoms segregated to the surface via the vacancy-mediated and the concerted mechanisms. These 24 Pd atoms migrate into the core and occupy the (100) facet sites of the truncated octahedral core (Figure 4b). No further Au-Pd core-shell segregation events were observed within the simulated  $3.8 \times 10^4$  s (11 hours). Instead, a large superbasin forms, corresponding to many surface rearrangements (see Figure S2) that hinder further segregation of Au atoms. The energy of the system decreases by 9.3 eV due to Au surface segregation, but the energy is still 20 eV higher than the global minimum structure, as determined from our MC simulations. For the random alloy system, the simulation started from a structure with 46 Au atoms on the NP surface (denoted as  $n=46$ ) with an energy 11 eV above the global minimum. The total energy of the random alloy NP decreases by 1.5 eV in  $1.2 \times 10^4$  s; very different from the staircase drop observed in the core@shell system. That is because the random alloy

system only undergoes surface rearrangement and not Au-Pd core-shell segregation. These surface rearrangements redistribute surface Au atoms to the corner and edge sites in the shell. Then, the system remains in a kinetically stable (trapped) state with the core structure and the number of surface Au atoms unchanged, showing no surface segregation in the  $3.8 \times 10^4$  s simulation time. These calculations reflect the high stability of the  $\text{Au}_{79}\text{Pd}_{122}$  random alloy NP at 400 K. In summary, although the core@shell is able to segregate Au to the surface and lower the energy, while the alloy NP cannot, both structures are kinetically trapped over experimental time scales.

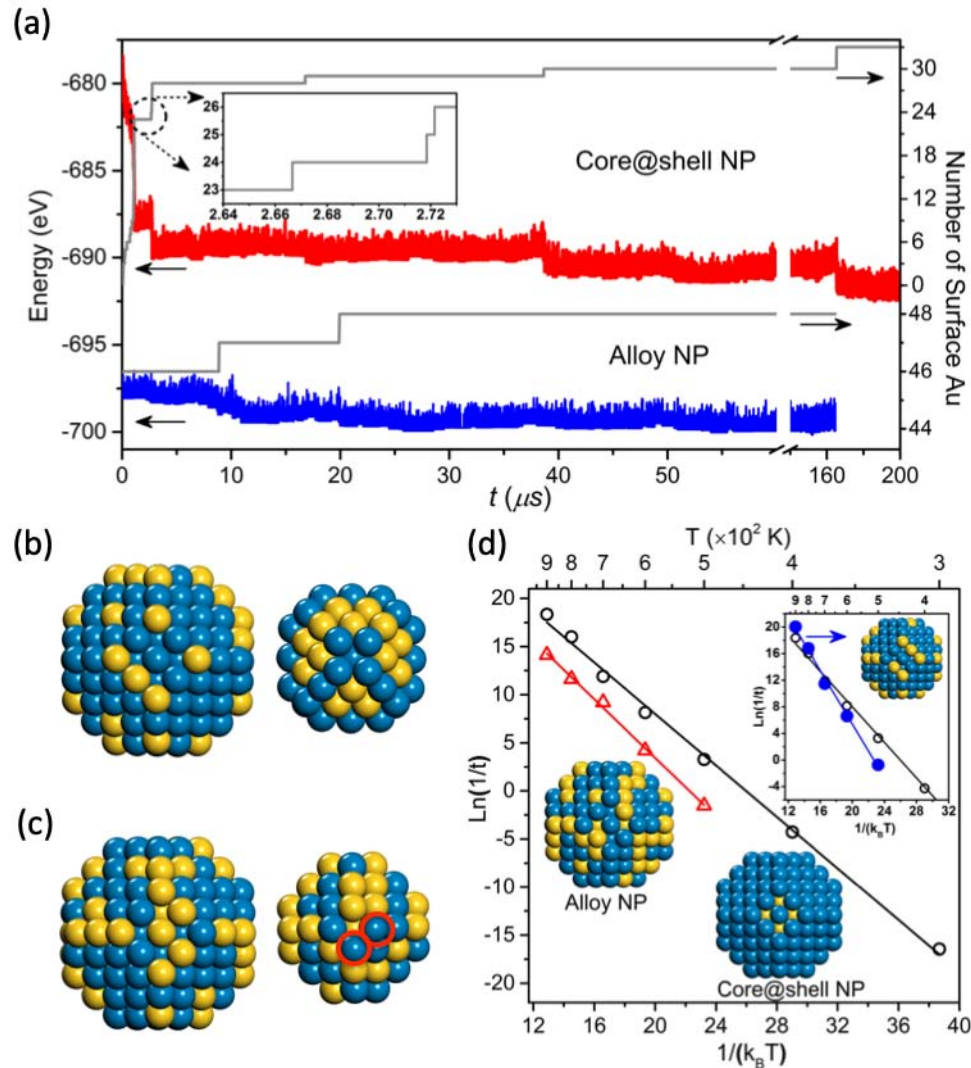


**Figure 5.** (a) Time evolution of the total energy (red and blue lines) and the number of surface Au atoms (grey lines) for AKMC simulations of the  $\text{Au}_{79}\text{Pd}_{122}$  core@shell (upper panel) and random alloy (lower panel) NP at 800 K. To show the escape process from the  $n=24$  state, the inset expands the 2.64 to 2.73  $\mu\text{s}$  portion of the plot. The minimum-energy structures with their corresponding

core structures for the (b) core@shell and (c) alloy NPs. (d) Arrhenius plots of the average segregation rate of the core@shell NP for  $n=0 \rightarrow 24$  (black, fit as ‘ $y = -1.34x + 34.75$ ’) and the alloy NP for  $n=46 \rightarrow 47$  (red, fit as ‘ $y = -1.53x + 33.95$ ’). The inset shows the average segregation rate of the core@shell NP for  $n=0 \rightarrow 24$  (black) and  $n=24 \rightarrow 25$  (blue, fit as ‘ $y = -2.01x + 40.69$ ’).

At temperatures above 400 K, surface segregation of Au atoms beyond the  $n=24$  kinetically trapped was observed for both the  $\text{Au}_{79}@\text{Pd}_{122}$  core@shell and random alloy NP. At 800 K, for example, the  $\text{Au}_{79}@\text{Pd}_{122}$  core-shell system reached the  $n=24$  state at 2.67  $\mu\text{s}$  (Figure 5a, inset); much faster than that at 400 K. Over the 200  $\mu\text{s}$  simulated, 34 Au atoms migrating to the NP surface, resulting in an energy drop of 12.92 eV. The same number of Pd atoms were exchanged into the core with 24 on the corner sites, nine on the edge sites and one occupying the corner site in the sub-layer of the core. Arrhenius plots for the  $n=0 \rightarrow 24$  and  $n=24 \rightarrow 25$  transitions are shown in the inset of Figure 5d. A comparison of the kinetics for these two transitions is key to understanding the origin of the kinetic trap observed at 400 K. The logarithm of the transition rate,  $\ln(1/t)$ , for both transition events show a linear relationship with  $1/(k_B T)$ . Note that a crossover above 700 K is observed in the Arrhenius plots, indicating a change in the segregation mechanism at this elevated temperature. Based on the Arrhenius law, an apparent activation energy of 1.34 eV is found for the  $n=0 \rightarrow 24$  transitions, whereas a higher activation energy of 2.01 eV is found for the  $n=24 \rightarrow 25$  transition. An examination of the transition mechanisms reveals that the higher barrier occurs from a highly defected truncated octahedral structure that facilitates the  $n=24 \rightarrow 25$  transition (shown in Figure S3), which is why the core@shell system is kinetically trapped in the  $n=24$  state at 400 K.

At 400 K, surface segregation of Au atoms in the random alloy NP is suppressed, in contrast to the fast segregation in the core@shell NP. The alloy NP is stable at 400 K and no surface segregation was seen in the simulated time scale of 200  $\mu\text{s}$ . Even at elevated temperatures, surface segregation in the random alloy system is very limited, qualitatively different from the rapid segregation in the core@shell NP. As shown in the lower panel of Figure 5a, only two Au atoms were observed to migrate to the surface at 800 K from the initial  $n=46$  state in the 165  $\mu\text{s}$  simulation time, corresponding to an energy decrease of 2.12 eV; significantly less than in the core@shell NP. To understand the origin of this difference, we constructed an Arrhenius plot for the first

segregation event in the random alloy NP, from state  $n=46 \rightarrow 47$ , as shown in Figure 5d (red line). The activation energy required for this transition is 1.53 eV; higher than for transitions required to reach the  $n=24$  state in the core@shell system. The higher activation energy limits surface segregation in the random alloy NP at 400 K.

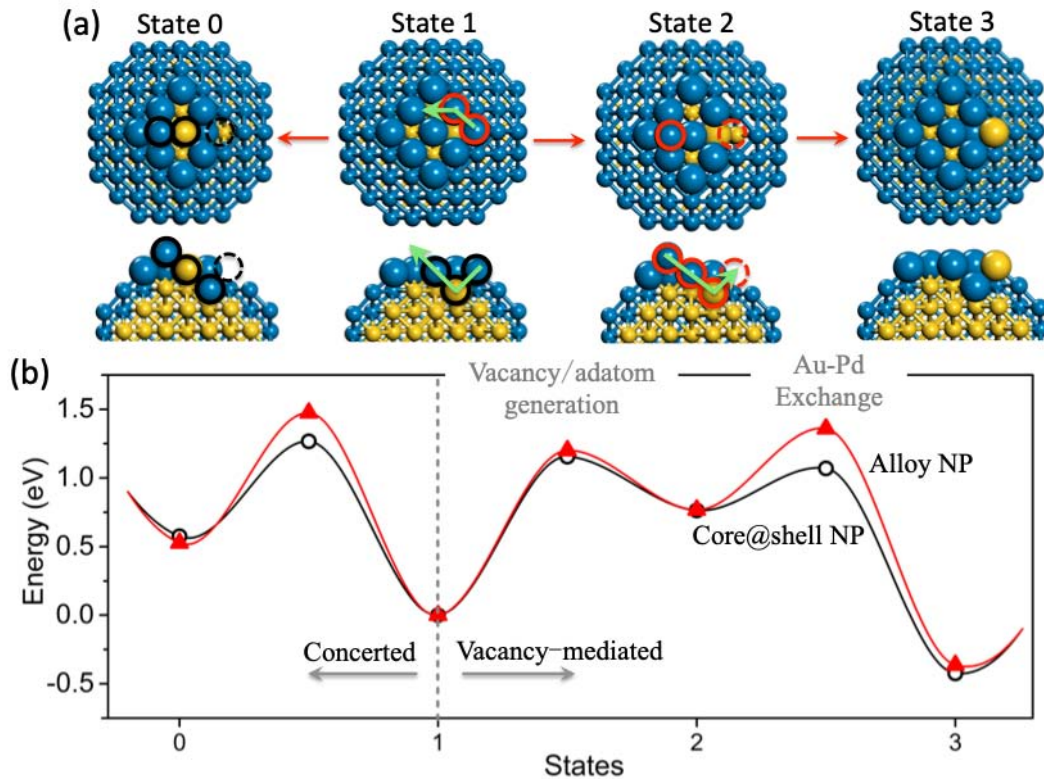


**Figure 6.** (a) Schematic illustration of the concerted (state 1 $\rightarrow$ 0) and the vacancy-mediated mechanism (state 1 $\rightarrow$ 3) in the Au<sub>79</sub>@Pd<sub>122</sub> core-shell NP. The corresponding schematic illustration for those in the Au<sub>79</sub>Pd<sub>122</sub> alloy NP is shown in Figure S4. (b) Energy profiles for Au segregation in the Au<sub>79</sub>Pd<sub>122</sub> core@shell (black line) and alloy NP (red line).

**Kinetic stability of the PdAu random alloy NP.** To understand the different segregation behaviors of the core@shell and random alloy NPs, we determined the segregation mechanisms by examining the AKMC trajectories. For both systems, surface segregation of Au occurs primarily on the (100) facet of the NP. For the core@shell NP, both the concerted and the vacancy-mediated mechanisms are active, but only the latter is observed in the random alloy NP. As shown in Figure 6a, the concerted mechanism undergoes direct Au-Pd exchange, without the prior formation of a vacancy, which occurs via the collective motion of three atoms along the direction indicated by the green arrow in the cross-section view of state 1. In contrast, and akin to that of

the  $\text{Au}_{19}\text{Pd}_{60}$  system, two sequential steps are involved in the vacancy-mediated mechanism – a vacancy-adatom formation step and the Au-Pd exchange step. Formation of the vacancy-adatom pair occurs via rearrangement of surface atoms on the (100) facet. Subsequently, a three-atom group (circled in the cross-section view of state 2) migrates along the direction indicated by the green arrow with the core Au atom filling the vacancy site and the shell Pd atom occupying the corner site of the core, completing the Au-Pd exchange process.

The energy profiles of these two mechanisms in the core@shell (black line) and the random alloy (red line) NPs are shown in Figure 6b. To the left of state 1 (gray dashed line) the concerted Au-Pd exchange in the core@shell NP has an energy barrier of 1.26 eV, whereas a higher barrier of 1.47 eV is required in the random alloy NP. In the vacancy-mediated mechanism, the vacancy-adatom formation step has a comparable energy barrier of 1.15 eV for the core@shell and 1.20 eV for the random alloy NP. A subsequent energy barrier of 0.60 eV is required for the Au-Pd exchange process in the alloy system – twice that of the core@shell system. Importantly, the overall barrier for Au segregation in the random alloy NP is 1.37 eV; 0.3 eV higher than that in the core@shell NP. This higher energy barrier dramatically lowers the segregation rate of Au atoms; specifically, the segregation rate in the alloy system is 1/6000 of that in the core@shell system at 400 K. This difference in the segregation energetics explains the suppression of segregation in the random alloy as compared to the core@shell NP.

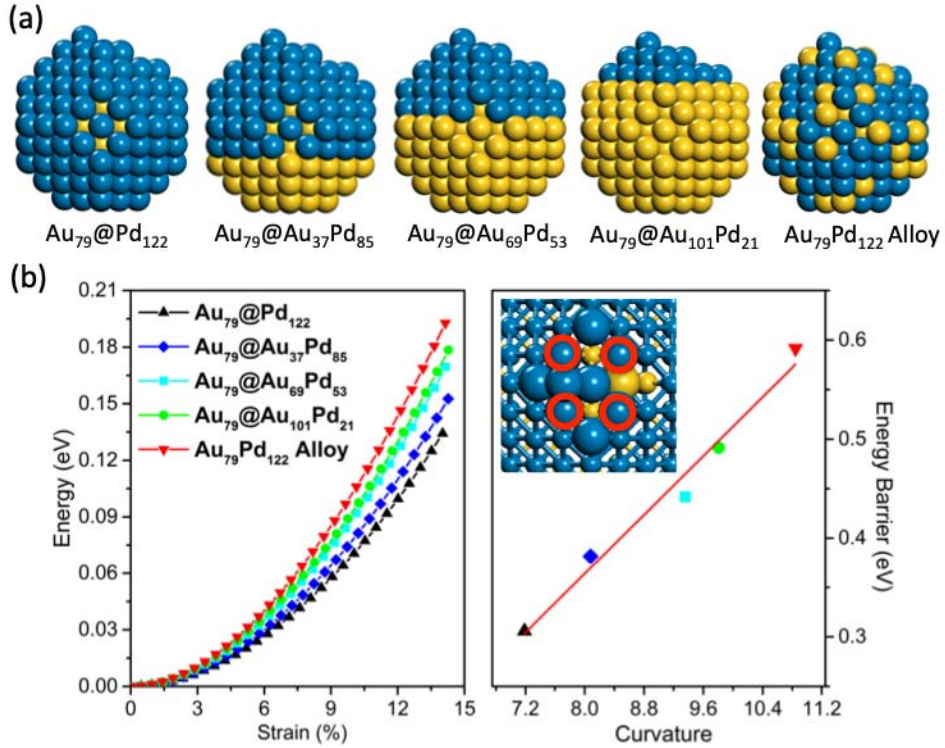


**Figure 7.** (a) Structures of the initial states of the Au-Pd exchange process (corresponding to state 2 in Figure 6a) via the vacancy-mediated mechanism in  $\text{Au}_{79}@\text{Pd}_{122}$ ,  $\text{Au}_{79}@\text{Au}_{37}\text{Pd}_{85}$ ,  $\text{Au}_{79}@\text{Au}_{69}\text{Pd}_{53}$ ,  $\text{Au}_{79}@\text{Au}_{101}\text{Pd}_{21}$  and  $\text{Au}_{79}\text{Pd}_{122}$  random alloy NPs. (b) Energy-strain curve (left panel) for each model presented in (a) is computed via linear interpolation between the initial and transition state. The strain is calculated as the percent expansion of the rectangular area surrounded by the circled atoms shown in the inset image. The right panel shows the strain dependence of the energy barrier for the Au-Pd exchange process.

While we have shown that the energy barriers for the Au-Pd exchange process are responsible for the different segregation behaviors in the random alloy and core@shell NPs, this does not provide an underlying reason for the differences in energy barriers. Surface energy is commonly assumed to be the main driving force for segregation. However, as shown in the energy profiles (Figure 6b), both systems have comparable reaction energies for the Au-Pd exchange step. That implies there are other factors determining the different kinetics in these two systems. In bimetallic NPs with metals of different sizes (such as Au and Pd) the induced strain is another important energetic factor. During the Au-Pd exchange process, there is a required expansion of the rectangular area defined by four Pd atoms, as highlighted by red circles in Figure 7b. The

energetic cost of such an expansion is directly related to the flexibility of the NP shell. A comparison of the pair distribution function in the particle shell indicates the  $\text{Au}_{79}\text{@Pd}_{122}$  core@shell NP is expanded (see Figure S5) due to the larger Au core in the core@shell NP. Hence, the strain effect may contribute to the different energy barriers observed in the core@shell and alloy NPs.

To explore the strain effect, we constructed three models, varying the number of Au atoms on the shell of the  $\text{Au}_{79}\text{@Pd}_{122}$  core@shell NP. Increasing the number of Au atoms in the shell reduces the strain in the shell, and modulates the local flexibility of the Pd group without changing the neighboring chemical environment. Energy variations of the strain are plotted in the left panel of Figure 7b, where the strain is defined as the % expansion of the rectangular area. As expected, with an increasing number of Au atoms in the shell, the NP energy increases faster with respective to the strain applied so that a larger curvature is observed, and a greater resistance to expansion. We further computed energy barriers for the Au-Pd exchange process via the vacancy-mediated mechanism for each system and plotted the curvature dependence of the energy barrier in the right panel of Figure 7b. The energy barrier for the Au-Pd exchange process increases linearly with the curvature. Notably, the alloy system has the largest curvature and requires the most energy for the Au-Pd exchange process, whereas the core@shell system has the smallest energy barrier because it has the most easily expandable shell. Therefore, we can conclude that the strain induced by the larger Au core in the core-shell NP drives surface segregation at the early stage, but the reduced flexibility of the alloy NP suppresses segregation due to strong Au-Pd interactions.

## Conclusions

The AKMC method has been used to model the evolution of PdAu NPs over experimental time scales. Surface segregation in both  $\text{Au}\text{@Pd}$  core@shell and PdAu alloy NPs were observed over time scales of seconds to hours that are unreachable by MD simulations. High segregation barriers in both systems point to kinetic trapping at energies well above equilibrium, which helps to resolve the experimental observation that both the core@shell and alloy NPs are found to be stable. A comparison of the kinetics between the two systems reveals the origin of the suppression of surface segregation in the PdAu alloy system; the shell of the alloy NP shell is less flexible than the core@shell NP, which increases the energy of the dominant segregation mechanism. Our study also demonstrates how the AKMC method can be applied to the important challenge of modeling the dynamics of bimetallic NPs over experimentally relevant time scales.

## Acknowledgements

This work was funded by ExxonMobil Research under project No. UTA17-000317 EM10480.13. Additional support was provided by the National Science Foundation under Grant CHE-1764230 and the Texas Advanced Computing Center for computational resources.

## Computational Methods

The AKMC method as implemented in the EON package was used to simulate the dynamical evolution of the core@shell and alloy AuPd NPs.<sup>53-55</sup> The energy and the force of the system were evaluated with the embedded atom method potential developed by Wadley.<sup>56</sup> High temperature at 2500 K MD simulations were used to explore possible reaction mechanism and product states. When each new state was found, the climbing image nudge elastic band (CI-NEB) method was used to determine the minimum-energy path connecting the current and new state through a saddle point.<sup>57,58</sup> The convergence criteria for the structure optimization and the CI-NEB method were set to 0.001 and 0.1 eV/ Å, respectively. At each new state, such high-temperature MD/CI-NEB cycles were repeated until a confidence value of 0.99 was reached for completeness of the rate table. The rate constant for each event was computed from the Arrhenius equation, ..., where,  $T$  and  $k_B$  are the energy barrier, temperature and the Boltzmann constant, respectively. The pre-exponential factor  $A$  was set as  $10^{13}$ /s for all simulations presented above. With all  $N_k$  possible transition events found for the state  $k$ , a rate table was constructed with the normalized cumulative function  $R_{k,i}$  where. At each KMC step, the  $i^{\text{th}}$  transition event was selected with a random number satisfying. The time was accumulated by, following first-order kinetics, where  $\Delta t$  was a second random number between 0 and 1. The absorbing Markov Chains method was used to improve simulation efficiency by analytically determining the escape time from superbasin states.<sup>59</sup>

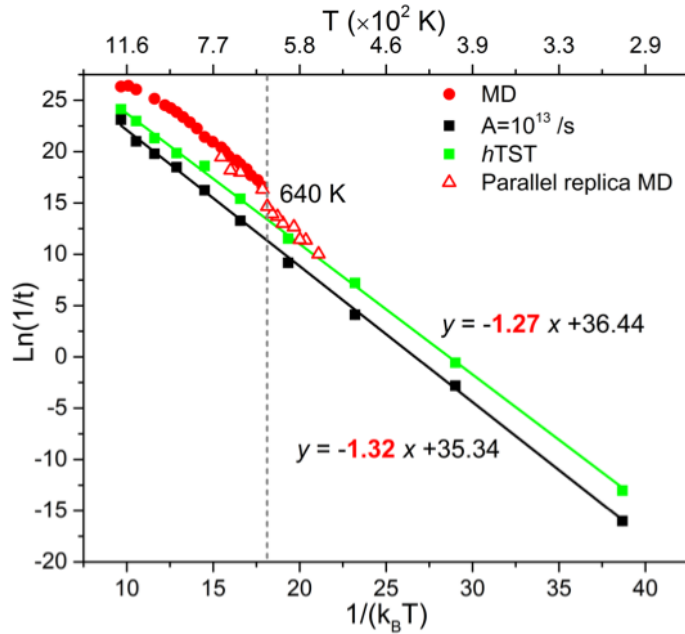


**Figure 8.** Arrhenius plots for the  $n=0\rightarrow 1$  transition obtained from MD and AKMC simulations. The black and the green dots represent data from AKMC simulations with  $A=10^{13}/\text{s}$  and explicitly calculated from *hTST* (...), respectively. The red circles and triangles are computed with conventional MD and parallel replica MD simulation, respectively.

To validate the methods used here, we compared the results of AKMC simulations with MD simulations in a high temperature range where a similar time scale can be achieved with both methods. Specifically, we compared the temperature dependence of the  $n=0\rightarrow 1$  transition, as shown in Figure 8. The transition time was averaged over 20 independent simulations for temperature. Due to the limited accessible time of the MD simulations, parallel replica MD simulations were used to extend the MD time scales at the lower temperatures.<sup>60</sup> We also performed AKMC simulations with pre-exponential factor calculated explicitly from harmonic transition state theory (*hTST*) where ..., and  $\omega_i$  and  $\omega_s$  are the normal mode frequencies of the initial and saddle point, respectively. We found that our assumed constant prefactor of  $10^{13}/\text{s}$  is systematically lower than prefactors calculated explicitly, by two orders of magnitude. Importantly, this means that our reported simulation time scales could have systematic errors on the order of two orders of magnitude. This difference, however, does not affect our conclusions because of the near-parallel relationship of the two Arrhenius plots. More importantly, at temperatures below 640 K, the results from replica MD simulations are consistent with those of our AKMC simulations. Deviations at

higher temperatures can be attributed to anharmonic effects that are not included in the AKMC simulations, but also not significant at the temperatures of interest in this study.

### **References:**

- (1) Chen, M. S.; Kumar, D.; Yi, C. W.; Goodman, D. W. The promotional effect of gold in catalysis by palladium-gold *Science* **2005**, *310*, 291.
- (2) Edwards, J. K.; Solsona, B.; N, E. N.; Carley, A. F.; Herzing, A. A.; Kiely, C. J.; Hutchings, G. J. Switching Off Hydrogen Peroxide Hydrogenation in the Direct Synthesis Process *Science* **2009**, *323*, 1037.
- (3) Sankar, M.; Dimitratos, N.; Miedziak, P. J.; Wells, P. P.; Kiely, C. J.; Hutchings, G. J. Designing bimetallic catalysts for a green and sustainable future *Chem. Soc. Rev.* **2012**, *41*, 8099.
- (4) Zhang, J.; Sasaki, K.; Sutter, E.; Adzic, R. R. Stabilization of platinum oxygen-reduction electrocatalysts using gold clusters *Science* **2007**, *315*, 220.
- (5) Ferrando, R.; Jellinek, J.; Johnston, R. L. Nanoalloys: From theory to applications of alloy clusters and nanoparticles *Chem. Rev. (Washington, DC, U. S.)* **2008**, *108*, 845.
- (6) Suntivich, J.; Xu, Z. C.; Carlton, C. E.; Kim, J.; Han, B. H.; Lee, S. W.; Bonnet, N.; Marzari, N.; Allard, L. F.; Gasteiger, H. A.; Hamad-Schifferli, K.; Shao-Horn, Y. Surface Composition Tuning of Au-Pt Bimetallic Nanoparticles for Enhanced Carbon Monoxide and Methanol Electro-oxidation *J. Am. Chem. Soc.* **2013**, *135*, 7985.
- (7) Maroun, F.; Ozanam, F.; Magnussen, O. M.; Behm, R. J. The role of atomic ensembles in the reactivity of bimetallic electrocatalysts *Science* **2001**, *293*, 1811.
- (8) Besenbacher, F.; Chorkendorff, I.; Clausen, B. S.; Hammer, B.; Molenbroek, A. M.; Norskov, J. K.; Stensgaard, I. Design of a surface alloy catalyst for steam reforming *Science* **1998**, *279*, 1913.
- (9) Rodriguez, J. A. Physical and chemical properties of bimetallic surfaces *Surf. Sci. Rep.* **1996**, *24*, 225.
- (10) Chen, M. S.; Luo, K.; Wei, T.; Yan, Z.; Kumar, D.; Yi, C. W.; Goodman, D. W. The nature of the active site for vinyl acetate synthesis over Pd-Au *Catal. Today* **2006**, *117*, 37.
- (11) Gao, F.; Goodman, D. W. Pd-Au bimetallic catalysts: understanding alloy effects from planar models and (supported) nanoparticles *Chem. Soc. Rev.* **2012**, *41*, 8009.
- (12) Stamenkovic, V. R.; Fowler, B.; Mun, B. S.; Wang, G. F.; Ross, P. N.; Lucas, C. A.; Markovic, N. M. Improved oxygen reduction activity on Pt3Ni(111) via increased surface site availability *Science* **2007**, *315*, 493.
- (13) Stamenkovic, V. R.; Mun, B. S.; Mayrhofer, K. J. J.; Ross, P. N.; Markovic, N. M. Effect of surface composition on electronic structure, stability, and electrocatalytic properties of Pt-transition metal alloys: Pt-skin versus Pt-skeleton surfaces *J. Am. Chem. Soc.* **2006**, *128*, 8813.
- (14) Alayoglu, S.; Zavalij, P.; Eichhorn, B.; Wang, Q.; Frenkel, A. I.; Chupas, P. Structural and Architectural Evaluation of Bimetallic Nanoparticles: A Case Study of Pt-Ru Core-Shell and Alloy Nanoparticles *ACS Nano* **2009**, *3*, 3127.
- (15) Loukrakpam, R.; Luo, J.; He, T.; Chen, Y. S.; Xu, Z. C.; Njoki, P. N.; Wanjala, B. N.; Fang, B.; Mott, D.; Yin, J.; Klar, J.; Powell, B.; Zhong, C. J. Nanoengineered PtCo and PtNi Catalysts for Oxygen Reduction Reaction: An Assessment of the Structural and Electrocatalytic Properties *J. Phys. Chem. C* **2011**, *115*, 1682.
- (16) Tao, F.; Grass, M. E.; Zhang, Y. W.; Butcher, D. R.; Renzas, J. R.; Liu, Z.; Chung, J. Y.; Mun, B. S.; Salmeron, M.; Somorjai, G. A. Reaction-Driven Restructuring of Rh-Pd and Pt-Pd Core-Shell Nanoparticles *Science* **2008**, *322*, 932.

(17) Xu, X. J.; Fu, Q.; Guo, X. G.; Bao, X. H. A Highly Active "NiO-on-Au" Surface Architecture for CO Oxidation *Ac<sub>s</sub> Catalysis* **2013**, *3*, 1810.

(18) Ahmadi, M.; Behafarid, F.; Cui, C. H.; Strasser, P.; Roldan Cuenya, B. Long-Range Segregation Phenomena in Shape-Selected Bimetallic Nanoparticles: Chemical State Effects *AC<sub>S</sub> Nano* **2013**, *7*, 9195.

(19) Mayrhofer, K. J. J.; Juhart, V.; Hartl, K.; Hanzlik, M.; Arenz, M. Adsorbate-Induced Surface Segregation for Core-Shell Nanocatalysts *Angewandte Chemie-International Edition* **2009**, *48*, 3529.

(20) Moscu, A.; Schuurman, Y.; Veyre, L.; Thieuleux, C.; Meunier, F. Direct evidence by in situ IR CO monitoring of the formation and the surface segregation of a Pt-Sn alloy *Chem. Commun. (Cambridge, U. K.)* **2014**, *50*, 8590.

(21) Andersson, K. J.; Calle-Vallejo, F.; Rossmeisl, J.; Chorkendorff, L. Adsorption-Driven Surface Segregation of the Less Reactive Alloy Component *J. Am. Chem. Soc.* **2009**, *131*, 2404.

(22) Brodsky, C. N.; Young, A. P.; Ng, K. C.; Kuo, C. H.; Tsung, C. K. Electrochemically Induced Surface Metal Migration in Well-Defined Core-Shell Nanoparticles and Its General Influence on Electrocatalytic Reactions *AC<sub>S</sub> Nano* **2014**, *8*, 9368.

(23) Gibson, E. K.; Beale, A. M.; Catlow, C. R. A.; Chutia, A.; Gianolio, D.; Gould, A.; Kroner, A.; Mohammed, K. M. H.; Perdjon, M.; Rogers, S. M.; Wells, P. P. Restructuring of AuPd Nanoparticles Studied by a Combined XAFS/DRIFTS Approach *Chem. Mater.* **2015**, *27*, 3714.

(24) Tao, F.; Grass, M. E.; Zhang, Y. W.; Butcher, D. R.; Aksoy, F.; Aloni, S.; Altoe, V.; Alayoglu, S.; Renzas, J. R.; Tsung, C. K.; Zhu, Z. W.; Liu, Z.; Salmeron, M.; Somorjai, G. A. Evolution of Structure and Chemistry of Bimetallic Nanoparticle Catalysts under Reaction Conditions *J. Am. Chem. Soc.* **2010**, *132*, 8697.

(25) Zugic, B.; Wang, L. C.; Heine, C.; Zakharov, D. N.; Lechner, B. A. J.; Stach, E. A.; Biener, J.; Salmeron, M.; Madix, R. J.; Friend, C. M. Dynamic restructuring drives catalytic activity on nanoporous gold-silver alloy catalysts *Nat. Mater.* **2017**, *16*, 558.

(26) de Bocarme, T. V.; Moors, M.; Kruse, N.; Atanasov, I. S.; Hou, M.; Cerezo, A.; Smith, G. D. W. Surface segregation of Au-Pd alloys in UHV and reactive environments: Quantification by a catalytic atom probe *Ultramicroscopy* **2009**, *109*, 619.

(27) Mayrhofer, K. J. J.; Hartl, K.; Juhart, V.; Arenz, M. Degradation of Carbon-Supported Pt Bimetallic Nanoparticles by Surface Segregation *J. Am. Chem. Soc.* **2009**, *131*, 16348.

(28) Pritchard, J.; Kesavan, L.; Piccinini, M.; He, Q.; Tiruvalam, R.; Dimitratos, N.; Lopez-Sanchez, J. A.; Carley, A. F.; Edwards, J. K.; Kiely, C. J.; Hutchings, G. J. Direct Synthesis of Hydrogen Peroxide and Benzyl Alcohol Oxidation Using Au-Pd Catalysts Prepared by Sol Immobilization *Langmuir* **2010**, *26*, 16568.

(29) Enache, D. I.; Edwards, J. K.; Landon, P.; Solsona-Espriu, B.; Carley, A. F.; Herzing, A. A.; Watanabe, M.; Kiely, C. J.; Knight, D. W.; Hutchings, G. J. Solvent-free oxidation of primary alcohols to aldehydes using Au-Pd/TiO<sub>2</sub> catalysts *Science* **2006**, *311*, 362.

(30) Gu, X. J.; Lu, Z. H.; Jiang, H. L.; Akita, T.; Xu, Q. Synergistic Catalysis of Metal-Organic Framework-Immobilized Au-Pd Nanoparticles in Dehydrogenation of Formic Acid for Chemical Hydrogen Storage *J. Am. Chem. Soc.* **2011**, *133*, 11822.

(31) Rostek, A.; Breisch, M.; Loza, K.; Garcia, P. R. A. F.; Oliveira, C. L. P.; Prymak, O.; Heggen, M.; Koller, M.; Sengstock, C.; Epple, M. Wet-Chemical Synthesis of Pd-Au Core-Shell Nanoparticles (8 nm): From Nanostructure to Biological Properties *Chemistryselect* **2018**, *3*, 4994.

(32) Zhang, L.; Niu, W. X.; Zhao, J. M.; Zhu, S. Y.; Yuan, Y. L.; Yuan, T.; Hu, L. Z.; Xu, G. B. Pd@Au core-shell nanocrystals with concave cubic shapes: kinetically controlled synthesis and electrocatalytic properties *Faraday Discuss.* **2013**, *164*, 175.

(33) Miller, H. A.; Bellini, M.; Vizza, F.; Hasenohrl, C.; Tilley, R. D. Carbon supported Au-Pd core-shell nanoparticles for hydrogen production by alcohol electroreforming *Catalysis Science & Technology* **2016**, *6*, 6870.

(34) Huang, X. X.; Shumski, A. J.; Zhang, X. Y.; Li, C. W. Systematic Control of Redox Properties and Oxygen Reduction Reactivity through Colloidal Ligand-Exchange Deposition of Pd on Au *J. Am. Chem. Soc.* **2018**, *140*, 8918.

(35) Li, Y. Y.; Hu, J.; Ma, D. D.; Zheng, Y. P.; Chen, M. S.; Wan, H. L. Disclosure of the Surface Composition of TiO<sub>2</sub>-Supported Gold Palladium Bimetallic Catalysts by High-Sensitivity Low-Energy Ion Scattering Spectroscopy *Ac<sub>s</sub> Catalysis* **2018**, *8*, 1790.

(36) Haire, A. R.; Gustafson, J.; Trant, A. G.; Jones, T. E.; Noakes, T. C. Q.; Bailey, P.; Baddeley, C. J. Influence of preparation conditions on the depth-dependent composition of AuPd nanoparticles grown on planar oxide surfaces *Surf. Sci.* **2011**, *605*, 214.

(37) Wang, L. L.; Tan, T. L.; Johnson, D. D. Configurational Thermodynamics of Alloyed Nanoparticles with Adsorbates *Nano Lett.* **2014**, *14*, 7077.

(38) Weir, M. G.; Knecht, M. R.; Frenkel, A. I.; Crooks, R. M. Structural Analysis of PdAu Dendrimer-Encapsulated Bimetallic Nanoparticles *Langmuir* **2010**, *26*, 1137.

(39) Christoffersen, E.; Stoltze, P.; Norskov, J. K. Monte Carlo simulations of adsorption-induced segregation *Surf. Sci.* **2002**, *505*, 200.

(40) Xiong, S. Y.; Qi, W. H.; Huang, B. Y.; Wang, M. P. Size-, Shape- and Composition-Dependent Alloying Ability of Bimetallic Nanoparticles *ChemPhysChem* **2011**, *12*, 1317.

(41) Deng, L.; Hu, W. Y.; Deng, H. Q.; Xiao, S. F. Surface Segregation and Structural Features of Bimetallic Au-Pt Nanoparticles *J. Phys. Chem. C* **2010**, *114*, 11026.

(42) He, X.; Zhang, S. E.; Cheng, F.; Chen, Z. X. The region-specific segregation and catalytic activity of gold-silver nanoparticles *Chem. Commun. (Cambridge, U. K.)* **2018**, *54*, 638.

(43) Soto-Verdugo, V.; Metiu, H. Segregation at the surface of an Au/Pd alloy exposed to CO *Surf. Sci.* **2007**, *601*, 5332.

(44) Paz-Borbon, L. O.; Johnston, R. L.; Barcaro, G.; Fortunelli, A. Structural motifs, mixing, and segregation effects in 38-atom binary clusters *J. Chem. Phys.* **2008**, *128*.

(45) Marchal, R.; Genest, A.; Kruger, S.; Rosch, N. Structure of Pd/Au Alloy Nanoparticles from a Density Functional Theory-Based Embedded-Atom Potential *J. Phys. Chem. C* **2013**, *117*, 21810.

(46) Yudanov, I. V.; Neyman, K. M. Stabilization of Au at edges of bimetallic PdAu nanocrystallites *Phys. Chem. Chem. Phys.* **2010**, *12*, 5094.

(47) Atanasov, I.; Hou, M. Equilibrium ordering properties of Au-Pd alloys and nanoalloys *Surf. Sci.* **2009**, *603*, 2639.

(48) Becker, O. M.; Karplus, M. The topology of multidimensional potential energy surfaces: Theory and application to peptide structure and kinetics *J. Chem. Phys.* **1997**, *106*, 1495.

(49) Doye, J. P. K.; Miller, M. A.; Wales, D. J. Evolution of the potential energy surface with size for Lennard-Jones clusters *J. Chem. Phys.* **1999**, *111*, 8417.

(50) Wales, D. J. *Energy landscapes: With applications to clusters, biomolecules and glasses*; Cambridge University Press: Cambridge, 2003.

(51) Evans, D. A.; Wales, D. J. Free energy landscapes of model peptides and proteins *J. Chem. Phys.* **2003**, *118*, 3891.

(52) Wales, D. J.; Miller, M. A.; Walsh, T. R. Archetypal energy landscapes *Nature* **1998**, *394*, 758.

(53) Henkelman, G.; Jonsson, H. Long time scale kinetic Monte Carlo simulations without lattice approximation and predefined event table *J. Chem. Phys.* **2001**, *115*, 9657.

(54) Xu, L. J.; Henkelman, G. Adaptive kinetic Monte Carlo for first-principles accelerated dynamics *J. Chem. Phys.* **2008**, *129*.

(55) Chill, S. T.; Welborn, M.; Terrell, R.; Zhang, L.; Berthet, J. C.; Pedersen, A.; Jonsson, H.; Henkelman, G. EON: software for long time simulations of atomic scale systems *Model. Simul. Mater. Sci. Eng.* **2014**, *22*.

(56) Foiles, S. M.; Baskes, M. I.; Daw, M. S. Embedded-Atom-Method Functions for the Fcc Metals Cu, Ag, Au, Ni, Pd, Pt, and Their Alloys *Phys. Rev. B* **1986**, *33*, 7983.

(57) Henkelman, G.; Uberuaga, B. P.; Jonsson, H. A climbing image nudged elastic band method for finding saddle points and minimum energy paths *J. Chem. Phys.* **2000**, *113*, 9901.

(58) Henkelman, G.; Jonsson, H. Improved tangent estimate in the nudged elastic band method for finding minimum energy paths and saddle points *J. Chem. Phys.* **2000**, *113*, 9978.

(59) Novotny, M. A. Monte-Carlo Algorithms with Absorbing Markov-Chains - Fast Local Algorithms for Slow Dynamics *Phys. Rev. Lett.* **1995**, *74*, 1.

(60) Voter, A. F. Parallel replica method for dynamics of infrequent events *Phys. Rev. B* **1998**, *57*, 13985.